High sensitivity 25μm and 50μm pitch microcantilever IR imaging arrays

Scott R. Hunter*, Gregory S. Maurer, Gregory Simelgor, Shankar Radhakrishnan, John Gray

Multispectral Imaging, Inc., 100 Misty Lane, Parsippany, NJ 07054

ABSTRACT

This paper reports on the development of small pixel pitch infrared FPAs based on the capacitively read bimorph microcantilever sensor technology. The heat sensing bimorph microcantilever structures are fabricated directly onto the CMOS control and amplification electronics to produce a high performance, low cost imager that is compatible with standard silicon IC foundry processing and materials. Positional responsivities of greater than 0.3 μm/K have been modeled and measured for 50 μm pitch pixels, corresponding to a temperature coefficient of capacitance, ΔC/C, (equivalent to TCR for microbolometers) above 30%/K. This responsivity, along with noise capacitances in the sub-attofarad range and nominal sensor capacitances of 15 fF, give modeled NEDT < 20 mK for these devices. Very preliminary infrared imagery has been obtained with a recently fabricated imaging array and assembled camera and control system, and indicates that NEDTs in 1 K range are presently being measured with this system. Considerable electronic noise is evident in the output response which, when eliminated, will lead to much reduced NEDT numbers in the near future. The measured thermal time constants for these arrays are in the 5 - 10 msec range.

At smaller pixel pitches, the positional responsivity decreases rapidly with feature size resulting in increased system NEDTs. Modeling the performance of microcantilever based IR sensors with innovative sensor structures and pixel pitches down to 17 μm indicates NEDTs < 20 mK and thermal time constants in the 5 msec range, are feasible with this technology. Results from detailed thermo-electro-opto-mechanical modeling of the operation of the 25 μm pitch pixels are presented.

Key Words: Infrared, thermal, bimorph, sensor, imager, MEMS, surface micromachining

1. INTRODUCTION

Infrared imaging sensors that operate without cryogenic cooling have the potential to provide commercial and military users with exceptional night vision capabilities packaged in a device of extremely small size, weight, and power. Considerable progress has been made in recent years reducing the pixel size while improving the camera sensitivity using current microbolometer imaging technology, but the present generation microbolometer 25 μm pitch pixel sensors have not been able to reach the sensitivity and time constant goals required by the military[1-4]. Next generation 17 μm pixel sensors will prove to be even more challenging using existing sensing technologies[5,6].

Multispectral Imaging (MII) is engaged in the development of an entirely new class of MEMS based uncooled infrared imaging detectors that have the potential to overcome the limitations of the present uncooled sensor technology and achieve superior performance[7]. This microcantilever technology utilizes a novel combination of surface micromachining techniques and the fabrication of the sensing elements directly on top of conventional low-power CMOS integrated circuits. This produces a bimaterial, thermally sensitive element that controls the position of a microcantilever capacitive plate coupled to the input of a low noise CMOS readout integrated circuit (ROIC).

Presented at the SPIE Defense and Security Symposium, April 11, 2007, and to be published in the SPIE Conference Proceedings Infrared Technology and Applications XXXIII, Vol. 6542

Microcantilever based IR detectors offer several distinct technical advantages over competing uncooled technologies:

- High temperature conversion sensitivity – MII has measured a temperature coefficient of capacitance (TCC, equivalent to temperature coefficient of resistance TCR for bolometers) > 30%/K for various sensor structures. The modeled performance can be much greater (up to 100%/K) depending on the required dynamic range.
- High dynamic range – true 14 bit dynamic range with a linear response at small signals and gap changes (up to ~ 0.2 µm corresponding to a temperature change of ~100K), and logarithmic response at large signals (up to 2,000K). The technology is capable of >16 bit operation up to 6,000K f/1 operation, but is limited by the ADC dynamic range and charge integration capacitance values.
- Low noise – there is no Johnson and 1/f noise in the sensor. The major noise terms are in the ROIC, namely the integration and charge transfer capacitors kT/C noise, and preamplifier and switching noise. Thermomechanical noise in the cantilever sensor is comparable to background thermal conductance noise for a properly tuned and damped sensor array.
- Snap shot operation with variable shutter speed and scene integration time (microseconds to milliseconds). There are no rolling shutter effects as with conventionally operated pulsed mode VO_x bolometers, leading to reduced aliasing and image smearing issues.

In addition, the use of 100% silicon IC-compatible processes to fabricate the MEMS sensor structures directly on the CMOS ROIC circuitry in large volume commercial MEMS fabrication facilities means that these sensor arrays can be fabricated with high yield and low manufacturing cost.

The IR sensor development efforts to date by MII have focused on the fabrication of 50 µm pitch pixels in a 160 x 120 imaging array, for use in cameras in the low cost, high performance commercial IR imaging markets. The basic operation of this detector array has been outlined in a previous paper[7]. In this paper, we briefly describe the operating principle of a capacitively read microcantilever based IR sensor along with the progress we have made in the fabrication of the 160 x 120 imaging arrays. The modeling and noise analyses we have performed to support the development of next generation 25 and 17 µm pitch sensor structures will also be summarized.

2. 25 MICRON PITCH MICROCANTILEVER IR SENSORS

The microcantilever sensor structure used in the present IR detector arrays, along with their operation in a capacitive bridge detection circuit, has been outlined in previous papers[7-10]. We will only highlight the operation of the bimaterial cantilever arm and how its structure and operation are modified to achieve high sensitivity operation at reduced pixel dimensions. Structural modifications have also been made to enable the sensor to be operated without a thermoelectric (TE) cooler to stabilize the sensor operating temperature.

a. Thermal Compensation Pixel Structure

A schematic diagram of a generic, capacitively sensed microcantilever sensor is shown in Figure 1. The microcantilever is attached electrically and mechanically to the substrate at one end by an anchor, and the cantilevered end is free to bend under the influence of changes in stress along the arm. One of the potential major drawbacks of the microcantilever sensor approach is that the sensor platform must be temperature stabilized otherwise the cantilever will respond to changes in the ambient temperature, producing drift and noise in the sensor output response. Incorporating a TE cooler in the sensor package to stabilize the sensor platform temperature adds cost, size, and power consumption in applications where minimization of these issues is essential.

Multispectral Imaging is developing a thermal compensation technique that minimizes the cantilever response to changes in the ambient temperature that was invented at the Oak Ridge National Laboratory (ORNL)[11]. The technique, shown schematically in Figure 2, adds a second bimorph and thermal isolation structure to the sensor. When these structure are incorporated in the design, both the IR sensing and additional structures respond identically but in opposite sense to the changes in ambient temperature, thus nulling out any substrate temperature induced motion in the cantilever paddle, and obviating the need for a (TE) cooler to maintain a constant paddle height even while the substrate varies in temperature. This structure has the added advantage that it also nulls out any mechanical bending of the bimorph and isolation arms due to residual stresses created during the sensor fabrication process. Extensive finite element modeling work by MII personnel and the experimental work of our ORNL colleagues shows that this structure compensates for substrate temperature fluctuations of 20^0C or more[11].

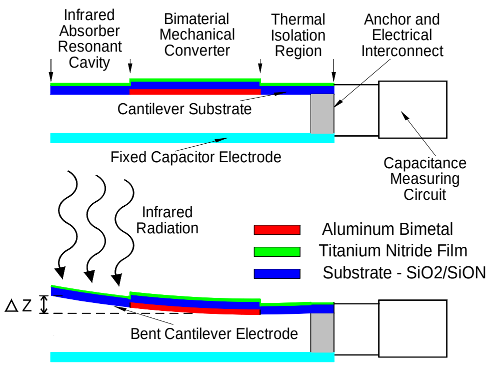

Figure 1. Schematic diagram showing the operating principle of the bimorph microcantilever IR sensor.

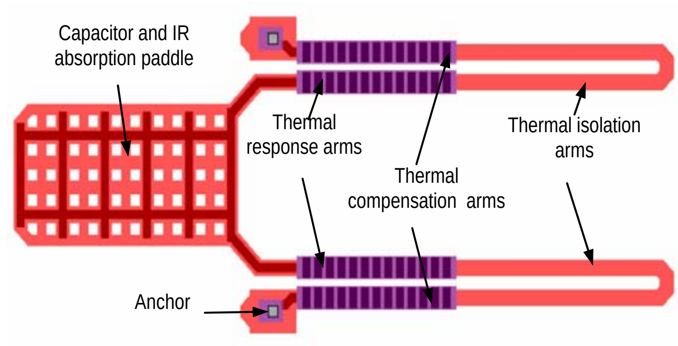

Figure 2. Schematic diagram of the thermally compensated 25 µm pixel pitch IR sensor structure.

b. Bimorph Structure

One of the more innovative features of the present sensor design is the shape of the temperature sensing bimorph structure[12], which is shown in the SEM image in Figure 3. The corrugated shape of this structure serves two purposes. First, it aids in binding together the various layers with which the sensor arm is fabricated. Delamination of these thin film structures is always a challenge for MEMS devices and the present structure prevents the films from sliding over one another due to temperature and processing induced stress changes in the films. Secondly, this structure has been found to considerably enhance the temperature positional responsivities ($\Delta z/\Delta T$) of the bimorph over that which would have been obtained for a flat structure of similar length. This structure has been shown to enhance the positional responsivity by a factor of 2-3, thereby greatly enhancing the bending response, enabling the attainment of lower operational NEDTs than for a flat bimorph structure. Measured responsivities for the 50 µm sensor structure shown in Figure 3 are in the range 0.30-0.40 µm/K while calculated values for a flat structure are in the range 0.1-0.12 µm/K. An SEM image from a section of a 50 µm pixel pitch imaging array incorporating the corrugated bimorph structure is shown in Figure 4.

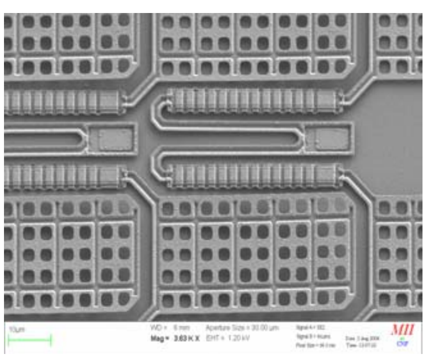

Figure 3. A scanning electron microscope (SEM) image of the corrugated bimorph structure used IR sensor.

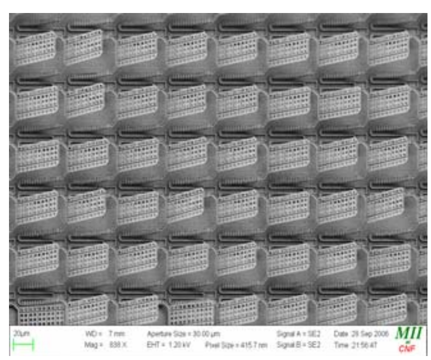

Figure 4. An SEM image showing the micro-cantilever pixels in a small section of the 160 x120 imaging array.

c. Bimaterial Cantilever Operation

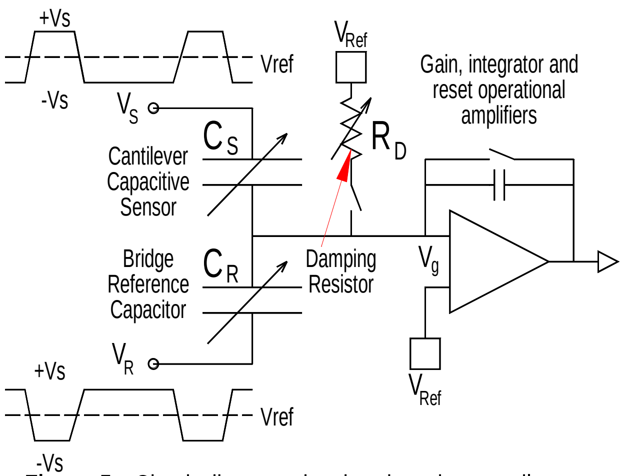

Figure 5. Circuit diagram showing the micro-cantilever bridge circuit, damping resistor and signal gain amplifier.

Figure 5 shows a schematic diagram of the operation of a capacitive bridge detector, with the variable plate microcantilever capacitive sensor forming one arm of the bridge circuit. The sensor is energized by applying symmetric, oppositely phased voltage pulses, $\pm V_S$, to the cantilever and bridge reference capacitors (C_S and C_R respectively) around a reference voltage, V_{Ref}. If the cantilever and bridge capacitances are the same size and V_S and V_R are of opposite sign (i.e. $C_S V_S = -C_R V_R$), then the voltage appearing at the common node between the capacitors is zero.

During operation, when the microcantilever sensor is exposed to the IR radiation, the paddle moves up, increasing the capacitor gap, thereby decreasing the sensor capacitance and generating an offset voltage, V_g, at the common node and at the input to the gain and integrator circuits (Figure 5). The deflection of the microcantilever tip, ΔZ, (Figure 1) when the sensor temperature increases from T_o to T due to the absorption of the IR radiation, is given by[13,14]:

$$\Delta Z = (3L_P^{\,2}/8t_{bi})(\alpha_{bi} - \alpha_{subs})(T - T_o)K_o \qquad (1)$$

where L_P is the length of the bimaterial section of the microcantilever sensor, α_{bi} and α_{subs} are the bimaterial (Al) and substrate material (SiO_2/SiON) thermal coefficients of expansion (TCE) respectively, t_{bi} is the thickness of the high TCE bimaterial, (T - T_o) is the differential absolute temperature, and the constant K_o is given by the following:

$$K_o = 8(1 + x)/(4 + 6x + 4x^2 + nx^3 + 1/nx) \qquad (2)$$

where $x = t_{subs}/t_{bi}$ is the ratio of the substrate to bimaterial thicknesses and $n = E_{subs}/E_{bi}$ is the ratio of the Young's moduli of the substrate and bimaterial. These equations indicate that the microcantilever bending, ΔZ, can be maximized by finding bimaterials with large differences in their thermal expansion coefficients and optimizing the cantilever sensor geometry.

The voltage responsivity (defined as volts/K) of the sensor is then given by:

$$R_V = \frac{V_S C_S}{C_T Z_{gap}} \frac{\Delta Z}{\Delta T} \qquad (3)$$

where Z_{gap} is the effective vacuum gap in the sensor and C_T is the sum of the total capacitances appearing at the input to the operational amplifier (including the sensor, reference, gate and parasitic capacitances).

A temperature coefficient of capacitance (TCC) may be defined for the microcantilever sensor which is analogous to the temperature coefficient of resistance (TCR) for thermoresistive microbolometers. The TCC is defined as follows:

$$TCC = \frac{1}{C_S} \frac{\Delta C}{\Delta T} = \frac{1}{Z_{gap}} \frac{\Delta Z}{\Delta T} \qquad (4)$$

d. Scaling Issues for 25 um Pitch Pixel Designs

When scaling the IR detector array to smaller pixel pitches, the pixel sensitivity is reduced by the same mechanisms as microbolometers (namely IR absorber area and isolation leg thermal conductance) and by the fact that a microcantilever sensor is an electromechanical device that depends on the physical dimensions of the structure for its mechanical advantage. Equations 1 and 2 show that the change in paddle height, ΔZ, is not only a function of the material properties of the bimaterial and substrate materials (namely the Young's moduli and TCEs) in a similar fashion to thermoresistive bolometers (electrical resistivity and TCR). The bending responsivity (defined as $\Delta Z/\Delta T$) is also a function of the dimensions of the cantilever structure.

This leads to the following scaling rules:

1. Reduced fill factor – scales as the pixel pitch squared – L^2
2. Reduced thermal isolation – scales as L
3. Reduced paddle responsivity from shorter bimaterial arm length – scales as L^2
4. Increased responsivity with thinner bimaterial – scales as $1/t_{bi}$
5. Increased responsivity with optimized bimaterial/substrate thickness ratio – Eq. 2
6. Increased responsivity with optimized Young's moduli ratio – Eq. 2
7. Increased TCC with decreasing effective vacuum gap – scales as $1/ Z_{gap}$

The first two rules are the same for bolometers and can be compensated for by reduced sensor fabrication design rules to tighten up the spacing between structures (giving a higher fill factor and increased thermal mass) and reduced thermal conductivity in the thermal isolation arms by reducing the interconnect metal thickness which largely controls the thermal conductivity when higher thermal isolation dielectric materials are used as the substrate material. Figures 6 and 7 show the scaling of the positional responsivity for a 25 μm pitch pixel structure similar to that shown in Figure 2 obtained from detailed thermo-electro-mechanical modeling of the expected sensor performance.

The positional responsivity of the pixel is plotted as a function of the bimetal film thickness in Figure 6 for several substrate film thicknesses. The solid black curve shows that for the substrate film thickness of 0.15 μm, the responsivity is optimized when the bimetal film thickness is around 0.75 μm.; i.e. around half the substrate film thickness. These curves also show that much higher responsivities can be achieved if the substrate film thickness is reduced. This has the added advantage of reducing the thermal capacity, reducing the thermal response time, but also increasing the thermal conductance noise. Thinner films however present sensor fabrication and infrared absorption issues, and there is ultimately a trade off between responsivity, thermal capacity, and thermal noise issues in the design of these devices.

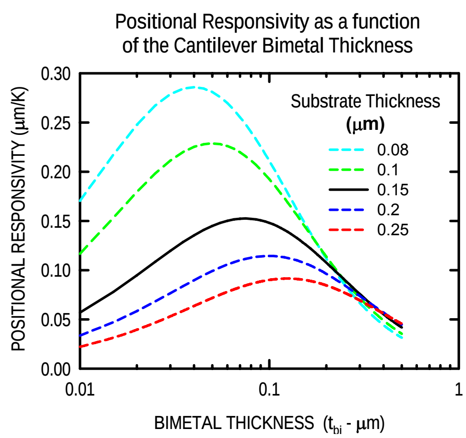

Figure 6. The positional responsivity of the 25 μm pitch pixel as a function of bimetal film thickness for several substrate film thicknesses.

The positional responsivity is plotted in Figure 7 as a function of both the ratio of the Young's moduli of the substrate and bimaterial film thicknesses (n) and the ratio of the ratio of these film thicknesses (x). The Young's moduli of the dielectric substrate materials (silicon oxynitrides) and the bimaterial (Al alloy) are very similar (≈ 70 GPa; i.e. n ≈1) for the thin film structures we are presently fabricating. The location of the responsivity of the modeled device is indicated by the red arrow on the surface of this plot. Again, there is considerable room for performance optimization adjusting the process conditions the stiffening the substrate material (which has the added advantage of raising the spring constant of the cantilever, increasing the resonant frequency and allowing higher operating voltages before pull-in issues become important[7,15].

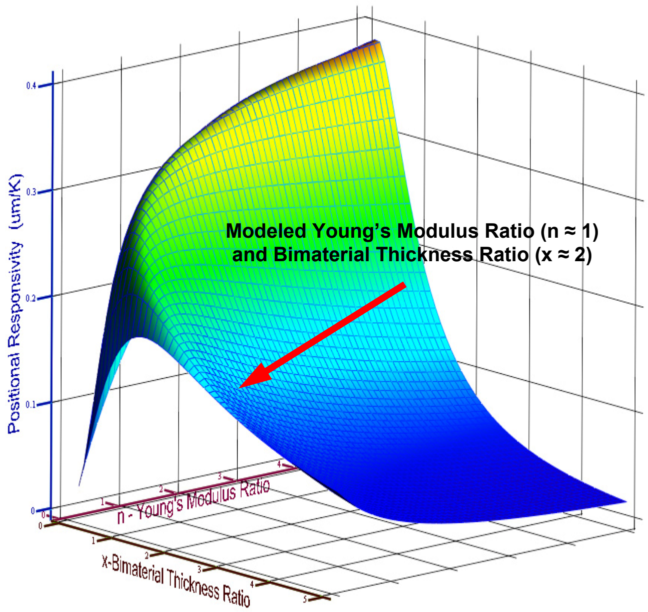

Figure 7. The positional responsivity of the 25 μm pitch pixel as a function of bimetal film thickness for several substrate film thicknesses.

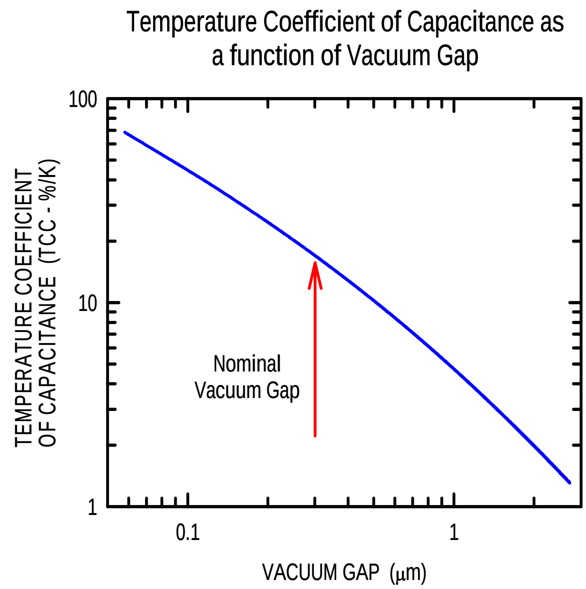

Figure 8. The calculated temperature coefficient of capacitance (TCC) for the 25 μm pixel design as a function of the sensor plate separation or vacuum gap.

The temperature coefficient of capacitance (TCC), defined in Eq. 4, is plotted in Figure 8 as a function of the vacuum gap. Also shown is the TCC for the 0.3 μm nominal vacuum gap. This particular design gives a TCC of 17%/K, but as the plot in Figure 8 shows, the TCC is strongly dependent on the cantilever and underlying sense plate separation.

Table 1. Sensor Dimensions and Values used to Model the NEDT Noise Values for a 50 μm, 25 μm, and 17μm Pixel Structure

Pixel Dimensions		50	25	17*
Leg Width	(μm)	3	1	1
Spacing	(μm)	2	0.8	0.5
Fill Factor		0.50	0.65	0.94
Emissivity	ε	0.85	0.85	0.9
Substrate Thickness	(μm)	0.25	0.15	0.08
Thermal Capacitance	(nJ/K)	0.92	0.13	0.051
Thermal Conductance	(nwatt/K)	90.4	17.7	11.8
Thermal Time Constant	(msec)	10.1	7.3	4.3
Vacuum Gap	(μm)	0.5	0.3	0.25
Bimetal responsivity	(μm/K)	0.27	0.15	0.19
Optical Transfer Coeff.	β	140	85	84
TCC	(%/K)	35	17	75
Pixel Capacitance	(fF)	15	8	9.6
Integration Capacitor	(fF)	320	420	420
*These modeled results are for an advanced pixel design not discussed in this paper				

Detailed modeling calculations have been performed on MII's existing 50 μm pixel design, the 25 μm pixel design shown in Figure 2, and an advanced 17 μm pixel design not described in this paper. The physical sensor structure dimensions and the measured (for the 50 μm pixel) and calculated (for the 25 μm and 17 μm pixel designs) positional responsivities (defined as ΔZ/ΔT) are shown in Table 1 along with the TCC values for these sensor designs. Using the enhanced sensitivity bimorph structure design described above, the measured and calculated TCC values for these designs are up to an order of magnitude or more greater than the values reported for either VO_x or a-Si thermo-resistive materials and will enable the microcantilever sensor to achieve NEDT values unattainable by other sensing means.

d. Thermal Response Time

The calculated thermal conductances G_{Th} (= $1/R_{Th}$ the thermal impedance) and thermal capacitances C_{Th} of the 50 μm, 25 μm and 17 μm sensor structures are also shown on Table 1. These values enable the sensor thermal time constant τ (defined as $\tau = C_{Th}/G_{th}$) to be calculated and they are also shown in Table 1 for a reasonable of sensor feature sizes (also summarized in Table 1). The thermal response times decrease with decreasing pixel pitch, as expected, due to the reduced length of the thermal isolation arms. This can be compensated for to some extent by decreasing the width and thickness of the isolation arm, but there are limits to the reduction in feature sizes that can be fabricated and still have a manufacturable sensor structure.

The thermal response times for the 25 μm pixel pitch design are shown in Figs. 9 and 10 as a function of the electrical interconnect and dielectric substrate thicknesses respectively, and for several isolation leg widths. The nominal leg width (1.0 μm) of the modeled sensor is shown as the solid black curve in these figures. Also highlighted is the thermal response time at the nominal design film thicknesses and leg width (τ = 7.3 msec).

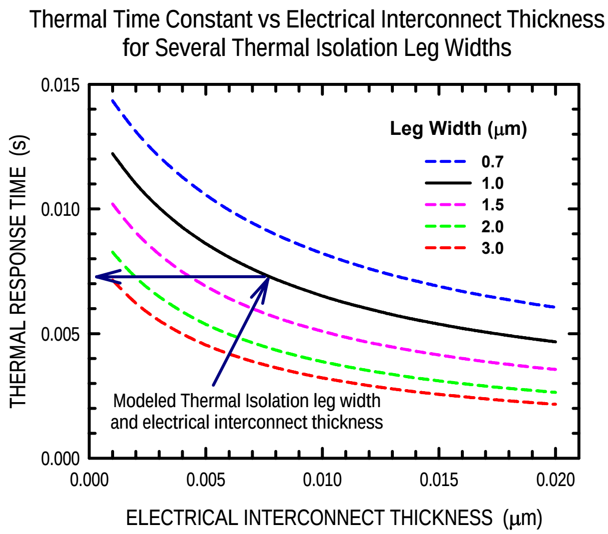

Figure 9. The thermal response time, τ, of the 25 μm pitch pixel as a function of the electrical interconnect metal thickness for several isolation leg widths.

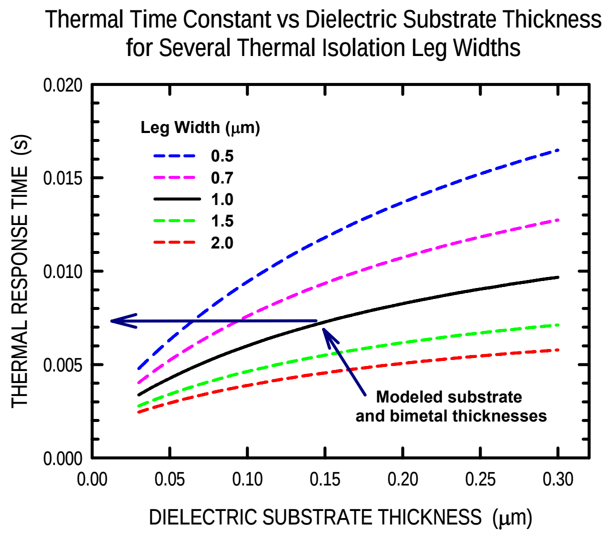

Figure 10. The thermal response time, τ, of the 25 μm pitch pixel as a function of the dielectric substrate thickness for several isolation leg widths.

e. Modeling - Noise Sources and Calculated Detector NEDT

The sources of noise in microcantilever based IR sensors and their influence on the system noise and resultant NEDT have been described in detail previously[7,8]. There are several noise sources associated with microcantilever based IR imagers; some present in all IR sensing techniques, while others specific to micromechanical based systems. The fundamental background limiting noise sources present in all IR radiation sensing systems are listed in Table 2, and are temperature or shot noise, and thermal conduction or fluctuation noise. In addition to these thermal noise sources, there are thermally driven noise sources that are specific to microcantilever sensors[16,17]. Microcantilever sensors are oscillating mechanical structures which store and exchange energy with their surroundings in the form of vibrational motion in the cantilever structure. This mechanical energy in the cantilever constitutes another source of thermally induced sensor noise.

Noise is also introduced in the signal chain at the detector, the readout and camera electronics, power supplies and other camera based noise sources. These noise sources are the ones which dominate in capacitively sensed thermal imaging systems and define IR camera performance limitations.

Table 2. Modeled NEDT Noise Values (mK) for a 50 µm, 25 µm and 17µm Pixel Structures			
Pixel Dimensions	50	25	17
Background Thermal Noise	1.2	2.1	3.5
Temperature Fluctuation Noise	5.2	7.3	10.4
Thermomechanical Noise	0.7	0.7	1.0
ROIC Noise Sources			
1/f + White Noise	9.7	7.4	7.4
kT/C Noise	7.0	8.7	15.1
Switching and other correlated noise	Small ?	Small ?	small ?
Total NEDT (mK)	13.1	13.7	19.8

Table 2 summarizes the NEDT values modeled for these various noise sources with the 50 µm, 25µm and 17 µm pitched pixels.

The dependence of the modeled NEDT from various sources for the 25 µm pitch pixel is plotted in Figure 11 as a function of the vacuum gap around the nominal operating position. The ROIC noise sources have been lumped into one value. The variation in the positional responsivity and the TCC with vacuum gap is primarily responsible the variation the ROIC NEDT. The other noise sources are independent of the sensor vacuum gap.

The curves in Figure 11 show that at the nominal plate separation of 0.3 µm, the system NEDT is around 15 mK or less. These calculations show that for all three pixel pitches, the ROIC noise is comparable in magnitude to the temperature fluctuation noise values and each of these pixel designs has the potential for sub 20 mK operation.

These noise sources include Johnson and 1/f noise in the on-pixel amplification and integration circuitry, k_BT/C noise in the charge integration capacitors, and various correlated on-chip switching noise sources and in the output signal chain. It is important to note that Johnson and 1/f noise sources are not present in pure capacitive sensors.

Using the responsivity, R_V defined by Eq. 3, these ROIC noise sources add in quadrature as follows:

$$NEDT_{ROIC} = \beta\sqrt{\Delta V_n^2 / R_V} \qquad (5)$$

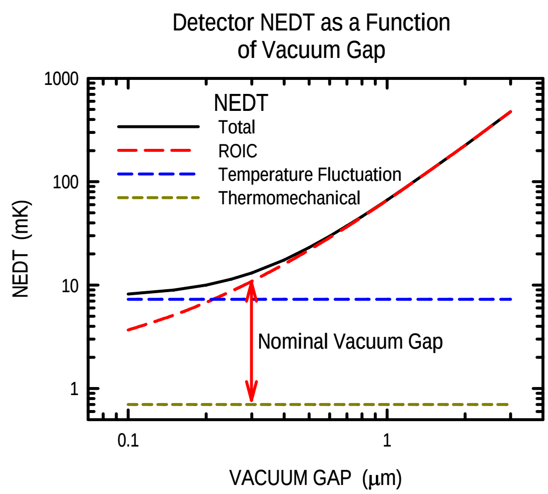

Figure 11. The Detector NEDT for a 25 µm pitch pixel as a function of the sensor plate separation.

3. FABRICATION OF 50 µm PITCH 160 x 120 PIXEL IR IMAGING ARRAYS

The design, modeling and operation of MII's 50 µm pitch microcantilever IR imaging detector arrays has been described in detail in an earlier paper[7]. In the present paper we describe the operation of the control electronics, detector packaging and camera operation of MII's first prototype camera, along with the very preliminary results MII has obtained with this camera.

a. IR Detector Array Fabrication and Packaging

Multispectral's first prototype focal plane imaging arrays (FPAs) are 160 x 120 pixel 50 µm pitch microcantilever arrays fabricated at the Cornell Nanoscience Facility (CNF) in Ithaca, New York. Figure 12 shows optical microscope images of two of these fabricated arrays with the array on the left being one of the best we have fabricated with a pixel yield >99%, and the one on the right showing a more typical array where pixels yields are in the 85-98% range. Figures 3 and 4 show SEM images of the details of the 50 µm pitch pixel structure (Figure 3) and several microcantilever pixel sensors from part of a larger imaging array (Figure 4). The images show that pixel structures can be fabricated that are flat to within approximately 1-2 microns, and just as importantly, they show very good reproducibility and mechanical uniformity from pixel-to-pixel.

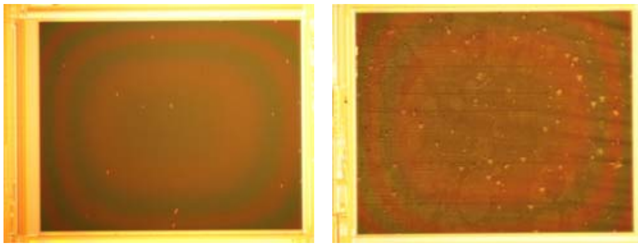

Figure 12. 160 x 120 imaging arrays fabricated at CNF showing a very high mechanical pixel yield device (left) with a yield>99%, and a more typical array with a 95% yield. The bright pixels are stuck to the substrate and thus inoperable.

For these first devices, pixel-to-pixel uniformities of better than ±5% are commonly achieved. The goal of the prototype development effort is to fabricate arrays with pixel yields >95% and paddle height uniformities to better than 5%. Capacitance variations from pixel-to-pixel due to paddle height variations smaller than this can be corrected using non-uniformity correction (NUC) capacitors in the sensor bridge circuit and electronically in the camera signal processing routines.

Figure 13 shows a schematic of the vacuum packaging we are using to house the detector array for our first laboratory and customer demonstration devices. This is a metal package with ceramic electrical feedthroughs and includes an antireflection coated germanium infrared transmitting window. A thermoelectric (TE) cooler is included to stabilize the temperature of the detector array along with a non evaporable getter to remove residual gas in the package after sealing. The height of the paddles in the array will vary with ambient temperature, so it's necessary to stabilize the temperature of the cantilever array so that the infrared image does not drift with temperature. The next generation pixel design described above will include a thermal compensation technique which will enable operation of the detector array without the TE cooler, reducing power consumption and cost.

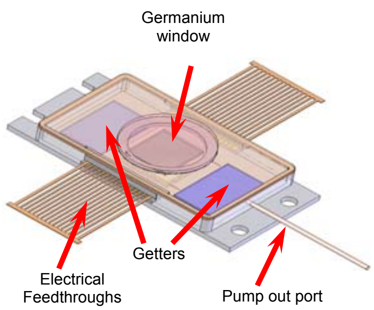

Figure 13. A schematic of a complete IR sensor package, including the antireflection coated germanium window, detector chip, thermoelectric cooler used to stabilize the temperature of the sensor chip, non evaporable getters, and the vacuum sealed sensor housing. The package is initially evacuated to approximately 10^{-6} torr to ensure that the sensor lifetime pressure does not rise above 10^{-3} torr during the life of the detector.

b. Customer Demonstration Alpha Camera Units

The microcantilever pixel sensing 160 x 120 pixel array ROIC has been designed, fabricated on 8" CMOS wafers using 0.25 µm mixed signal design rules, and the resulting ROIC die mounted in open face test packages and the CMOS functionality tested using dedicated sensor test electronics. These tests confirmed that the ROIC is functioning as designed. Specifically, noise capacitances of 1 attofarad (10^{-18} F) using test capacitors have been obtained. This translates into a NEDT for the readout electronics of around 20 mK. These are initial noise values which will improve with better shielding and circuit operation optimization. Based on these results, parasitic capacitances in the readout circuit, which were a problem during a previous attempt to fabricate capacitive microcantilever IR detector arrays[8], have been modeled correctly and will not be an issue for the present devices.

Complete IR Alpha evaluation cameras have been designed and fabricated, and are presently undergoing debugging and optimization. A schematic diagram of the Alpha system unit and board layout is shown in Figure 14. The system includes an IR camera unit based around an Electrophysics PV320A IR camera box and separate camera control and data analysis unit designed by D3 Engineering[18]. The camera unit contains a three board set (shown in Figure 15); they being a detector board, CPLD microprocessor control board, and a TE controller and power supply board. A picture of the camera box, with the top lid removed to expose the internal board layout, is shown in the left image in Figure 16, and the camera unit located on top of the camera control unit is shown in right image in Figure 16.

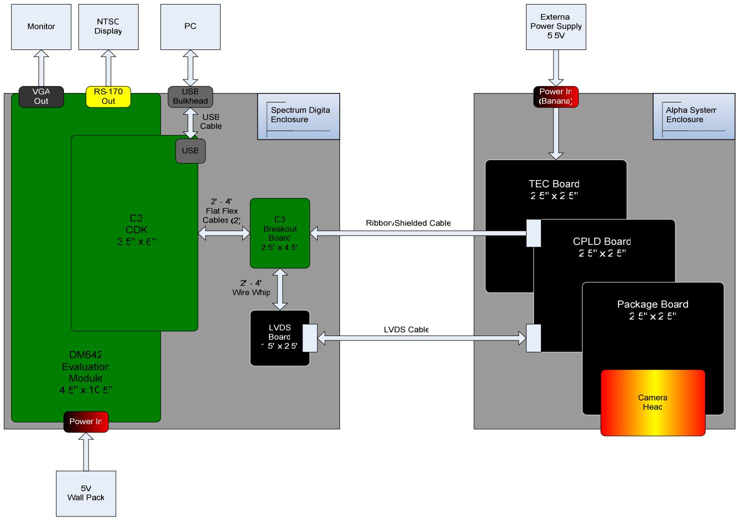

Figure 14. A schematic of the Alpha camera system, showing the 3 electronics boards located in the Camera unit (right) and camera control unit (left) and the control and data communication lines).

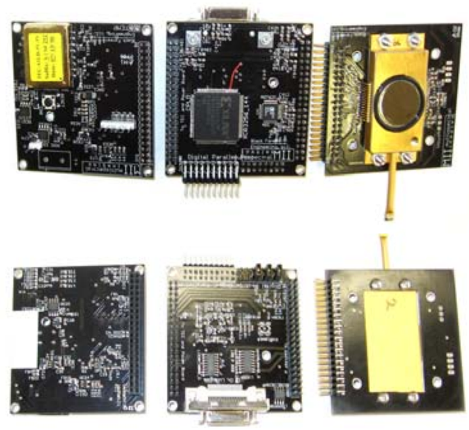

Figure 15. The Alpha camera system 3 electronics board set located in the Camera unit. From right - the detector board, the CPLD board and the TE controller board.

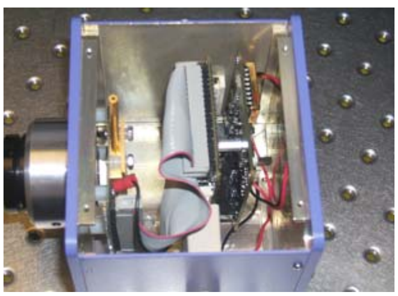

Figure 16. (Left) - One of several Alpha camera units containing the 3 electronics board set that have been fabricated to test the operation and functionality of the detector arrays, and (Right) - The camera box located on top of the camera control box. The LVDS communications cable is also shown.

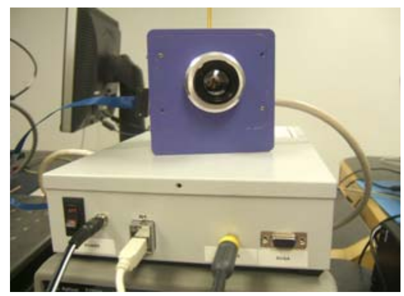

c. Camera Test Setup

Figure 17 shows an Alpha system camera unit located in front of a Santa Barbara Infrared (SBIR)[19] 14000 Series infrared target projector test system. The detector located within this camera was an open port design and is shown coupled to an external vacuum system. This arrangement allows us to study the effect of back fill gas pressure on the performance of the FPAs under test. Pinched off FPAs containing getters are also under test to determine vacuum and getter lifetime issues.

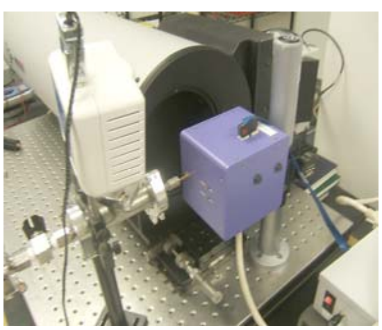

Figure 17. The Alpha system camera head located in front of the Santa Barbara Infrared target projector. The FPA under test is coupled to a vacuum system shown to the left of the image.

A calibrated black body source in the projector was used in the system noise measurements and either an f/1.6 or f/0.87 germanium lens was used to focus the black body radiation from the projector onto the detector array. The array under test was connected to the drive and sense electronics in the camera unit (Figure 16). Multiplexed analog and digital output data was fed into the camera control unit and digital scope. The processed data was fed into an external monitor for viewing or a control computer for further analysis.

A FLIR Omega[20] camera was tested using the SBIR test system and the measured NEDTs obtained using the SBIR standard test routines gave NEDT values consistent with the published specifications for this camera.

c. Infrared Imagery

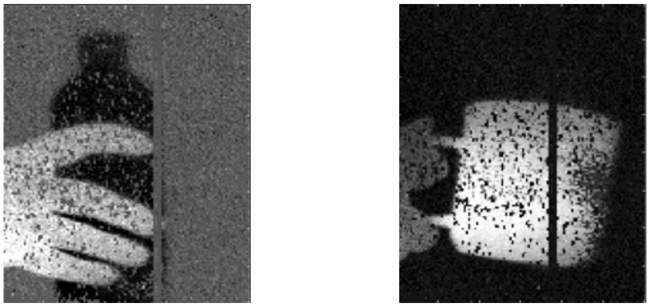

Figure 18. Two images captured by a frame grabber, and taken directly from the 50 Hz video output from the IR engine. The only processing on these images was a non uniformity correction to correct variations in the background. The working pixel yield on this packaged detector was around 85%.

MII has recently fabricated the first batches of fully integrated 160 x 120 imaging arrays. The observed pixel functionality from these early batches of FPAs typically range in functionality from 80% to >95%. These arrays are fabricated at the Cornell Nanoscale Science and Technology Facility (CNF) in a multi-user facility environment. MII has an ongoing development program with Dalsa Semiconductor to commercialize this technology. Dalsa has a much cleaner and reproducible fabrication environment, and consequently, we fully expect pixel yields to be >99% when in full production.

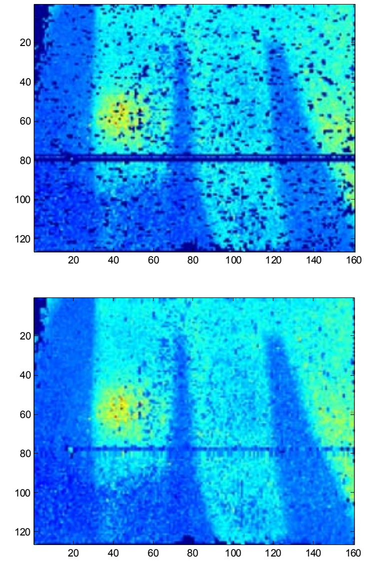

Figure 19. A dead pixel substitution routine has been recently implemented in our image non-uniformity routines. These images show the effect of substituting nearest neighbor pixels for the non functional pixels in the array.

Some preliminary IR imaging obtained with these arrays is shown in Figure 18 where the left image is of a hand holding a cold water bottle and the right image is of a hand holding a hot coffee mug. A non uniformity correction has been applied to these images to remove variations in background signal levels due to paddle height variations in the array. There is a column defect in this particular array near the center of the image. Row and column defects are present in around 5% of the arrays that have been examined so far. In Figure 19, a nearest neighbor pixel substitution routine has been applied to non-responding pixels to the image of a hand (presumably sensor paddles that are stuck to the substrate), showing that considerable improvements in image quality are possible with processed images.

These images and other measurements we have performed indicate that the NEDT values for these arrays, under typical operating conditions, are around 1K, much higher than the modeling and sensor structure measurements indicate that these sensors are capable of. Analysis of the sensor analog and digital outputs shows the presence of high levels of electronic noise, specifically clock pulse feedthrough. The camera and control units are presently being debugged and we expect to reduce the noise levels from these sources by two orders of magnitude or more, considerably improving the detector NEDTs values.

d. Thermal Response Time Measurements

Direct accurate measurements of the thermal response time of the fabricated imaging arrays have not been measured at this time. Detailed modeling of the thermomechanical response of the pixels in an imaging array give thermal response times in the 5-10 msec range. Similarly, direct measurement of the motion of MII's microcantilever paddle structures after transient excitation by a pulsed IR laser, by our colleagues at ORNL[22], also give response times in the 5-10 msec range. Thus, along with the observation that we observe negligible image smearing for rapidly moving IR scenes, we conclude the response times for the present imaging arrays are in this thermal response time range.

e. NEDT Measurements

The noise equivalent temperature difference (NETD) for a thermal imaging array can be determined from the following relationship:

$$\mathrm{NETD} = \frac{V_{Noise(rms)}[\mathrm{mV}]}{R\,[\mathrm{mV}/^{0}\mathrm{C}]} \qquad (6)$$

where $V_{Noise(rms)}$ is the focal plane array readout noise and R is the system responsivity. The responsivity R is found by first obtaining the conversion gain for the imaging array. The output voltages from the array are obtained from 50 frames of data at two black body source temperatures (usually 1-5^{0}C apart). The differences in the two output voltages are divided by the difference in the average digitized A/D converter units (ADU's) to obtain the conversion gain (in mV/ADU) on a pixel-by-pixel basis. The responsivity is then computed by dividing the change in ADU's by the temperature difference and multiplying the result by the conversion gain to obtain the responsivity (in mV/^{0}C) for each pixel in the array.

$$R_{\,[\mathrm{mV}/^{o}\mathrm{C}]} = \frac{\mathrm{ADU}_2 - \mathrm{ADU}_1}{\Delta T} \times \text{Conversion Gain}_{\,[\mathrm{mV/ADU}]} \qquad (7)$$

The readout noise $V_{Noise(rms)}$ is found by acquiring a number of image frames (usually 64 or 128) with a frame grabber and computing the true rms variation in (ADU's) for each pixel and multiplying the result by the conversion gain for the A/D unit, in mV/ADU, to obtain the noise voltage in mV (rms) per pixel. The measured noise value for each pixel is recorded and plotted in a histogram to determine the average noise for the entire focal plane array. Histograms of the NETD for the pixels in the array are then obtained, from which the average array NETD may be obtained.

An important feature of microcantilever capacitive sensors is that the sensitivity and dynamic range of the devices is dependent on the paddle height, and hence operating temperature of the detectors. As the temperature increases, the paddles move further away from the surface of the detector decreasing the pixel capacitance and sensitivity (and consequently lowering the NETD of the detector) with the paddle orientation used in the present devices. This in contrast to an earlier effort[8] where the paddles moved closer to the substrate with increasing temperature. The advantage of the present orientation is that cantilever "pull-in" is minimized and the dynamic range of the output response greatly increased[7,8,15,21].

Although NEDT histograms from a commercially available FLIR Systems Omega camera have been made on the SBIR IR target projector system discussed above, and give consistent and repeatable results, consistent and reliable sets of measurements have yet to be made on MII's first imaging arrays. Such measurements are expected shortly once the majority of the observed electronic noise in the sensor output response has been eliminated

ACKNOWLEDGEMENTS

Many people have contributed directly and indirectly to the work outlined in this paper. We particularly wish to thank our colleagues at Black Forest Engineering and D3 Engineering for their support in the design and testing of the ROIC and test electronics, the staff and researchers at the Cornell Nano Science and Technology Fabrication Facility, Martin Bauer and our colleagues at the Oak Ridge National Laboratory for testing and measuring the performance parameters of several of the microcantilever sensor structures.

Multispectral Imaging also wishes to acknowledge the support of the US Army through an SBIR grant for part of this work.

* shunter@multispectral.net www.multispectral.net

REFERENCES

1. Fraenkel, A. et al. "VOx-Based Uncooled Microbolometric Detectors: Recent Developments at SCD" in *Infrared Technology and Applications XXXII* (ed. Andresen, B. F., Fulop, G. F. and Norton, P.R.) 62061C-1 (SPIE, Orlando, FL, 2006).
2. Murphy, D. F. "High sensitivity 640 x 512 (20µm pitch) microbolometer FPAs" in *Infrared Technology and Applications XXXII* (ed. Andresen, B. F. a. F., G. F.) (SPIE, Orlando, FL, 2006).
3. Norton, P. W. "Uncooled thermal imaging sensor and application advances" in *Infrared Technology and Applications XXXII* (ed. Andresen, B. F. a. F., G. F.) (SPIE, Orlando, FL, 2006).
4. Tissot, J. L. et al. "First Demonstration of 640x480 Uncooled Amorphous Silicon IRFPA with 25 um pixel-pitch" in *Infrared Technology and Applications XXXII* (ed. Andresen, B. F., Fulop, G. F. and Norton, P.R.) 620618-1 (SPIE, Orlando, FL, 2006).
5. Hanson, C. M. ''Barriers to background-limited performance for uncooled IR sensors" in *Infrared Technology and Applications XXX* (eds. Bjørn F. Andresen & Fulop, G. F.) 454-464 (SPIE, Orlando, Florida, 2004).
6. Kohin, M. & Butler, N. "Performance Limits of Uncooled VOx Microbolometer Focal Plane Arrays" in *Infrared Technology and Applications XXX,* (eds. Andresen, B. F. & Fulop, G. F.) 447-453 (SPIE, Orlando, Florida, 2004).
7. Hunter, S. R., Maurer, G., Jiang, L. & Simelgor, G. "High Sensitivity Uncooled Microcantilever Infrared Imaging Arrays" in *Infrared Technology and Applications XXXII* (ed. Andresen, B. F., Fulop, G. F. and Norton, P.R.) 62061J-1-12 (SPIE, Kissimmee, Florida, USA, 2006).
8. Hunter, S. R. et al. "High Sensitivity Uncooled Microcantilever Infrared Imaging Arrays" in *Infrared Technology and Applications XXIX* (eds. Andresen, B. F.) 469-480 (SPIE, Orlando, FL, 2003).
9. Amantea, R. et al. "Progress towards an Uncooled IR Imager with 5 mK NEDT" in *Infrared Technology and Applications XXIV* (ed. Andresen, B. F.) 647-659 (SPIE, San Diego, CA, 1998).
10. Amantea R., Knoedler C. M., Pantuso F. P., Patel V. K., Sauer D. J. and Tower J. R., "Uncooled IR imager with 5mK NETD", *Proc. Infrared Technology and Applications XXIII,* SPIE Vol. 3061, pp. 210-222, (Orlando, FL, 1997).
11. Corbeil, J. L., Lavrik, N. V., Rajic, S. & Datskos, P. G. "Self-leveling uncooled microcantilever thermal detector." *Appl. Phys. Lett.* **81**, 1306-1308 (2002).
12. Simelgor, G. & Hunter, S. R. "Apparatus Comprising a Thermal Bimorph with Enhanced sensitivity." US Patent Applied for (Multispectral Imaging, Inc., USA, 2006).
13. Shaver, P. J. "Bimetal Strip Hydrogen Gas Sensor." *Rev. Sci. Instrum.* **40**, 901-905 (1969).
14. Young, W. C. *Roark's Formulas for Stress and Strain* (McGraw-Hill, New York, 1989).
15. Varghese, M., Amantea, R., Sauer, D. J. & Senturia, S. D. "Resistive Damping of Pulsed-Sensed Capacitive Position Sensors" in *1997 Int. Conf. Solid-State Sensors and Transducers - Transducers '97* 1121-1124 (IEEE, Chicago, IL, 1997).
16. Sarid, D. *Scanning Force Microscopy* (Oxford University Press, New York, 1994).
17. Cunningham, J. P., Rajic, S., Datskos, P. & Evans, B. M. US Patent 6,805,839 (2004).
18. D3 Engineering website - www.d3engineerng.com
19. Santa Barbara Infrared website - www.sbir.com
20. FLIR Systems website - www.flir.com
21. Senturia, S. D. *Microsystem Design* (Kluwer Academic Publishers, Boston, 2001)
22. Lavrik, N. V., Grbovic, D., Rajic, S., Datskos, P. G., Forraai, D., Nelson, E., Devitt, J., and McIntyre, B. "Uncooled infrared imaging using bimaterial microcantilever arrays" in *Infrared Technology and Applications XXXII* (ed. Andresen, B. F., Fulop, G. F. and Norton, P.R.) 62061J-1-12 (SPIE, Kissimmee, Florida, USA, 2006).